Fluorine Aided Stabilization of Pt Single Atoms on TiO_2 Nanosheets and Strongly Enhanced Photocatalytic H_2 Evolution

Si-Ming Wu,[†] Imgon Hwang,[†] Benedict Osuagwu,[†] Johannes Will,[‡] Zhenni Wu,[†] Bidyut Bikash Sarma,[‖] Fu-Fei Pu,[+] Li-Ying Wang,[§] Zdenek Badura,[Δ] Giorgio Zoppellaro,[Δ] Erdmann Spiecker,[‡] and Patrik Schmuki[†Δ±]*

[†]Department of Materials Science WW4-LKO, University of Erlangen-Nuremberg, Martensstraße 7, 91058 Erlangen, Germany

[‡]Institute of Micro- and Nanostructure Research & Center for Nanoanalysis and Electron Microscopy (CENEM), University of Erlangen-Nuremberg, IZNF, Cauerstraße 3, 91058 Erlangen, Germany

[‖]Institute of Catalysis Research and Technology (IKFT) and Institute for Chemical Technology and Polymer Chemistry (ITCP), Karlsruhe Institute of Technology (KIT), Hermann-von-Helmholtz-Platz 1, 76344 Eggenstein-Leopoldshafen, Germany

[+]School of Materials Science and Engineering, Wuhan University of Technology, Wuhan, 430070, China.

[§]State Key Laboratory of Magnetic Resonance and Atomic and Molecular Physics, Wuhan Institute of Physics and Mathematics, The Chinese Academy of Sciences, Wuhan, 430071, China

[Δ]Regional Centre of Advanced Technologies and Materials, Šlechtitelů 27, Olomouc 78371, Czech Republic

[±]Department of Chemistry, Faculty of Science, King Abdulaziz University, P.O. Box 80203, Jeddah 21569, Saudi Arabia

KEYWORDS: Single atom platinum, dark deposition, photocatalysis, surface fluorination, titanium dioxide

ABSTRACT: Trapping sites in single atom (SA) catalysts are critical to the stabilization and reactivity of isolated atoms. Herein, we show that anchoring of Pt SAs on TiO_2 nanosheets is strongly aided by lattice incorporated fluorine species. Tailoring the speciation of fluorine on TiO_2 nanosheets is a key factor for uniform and stable dispersion of the Pt SAs and high efficiency in Pt SA co-catalyzed photocatalytic H_2 production. Fluorine-stabilized uniformly dispersed Pt SAs on the (001) surface of TiO_2 can provide a remarkable photocatalytic activity (a H_2 production rate of 45.3 mmol $h^{-1}mg^{-1}$ Pt for 65 mW/cm^2 365 nm light). This high (maximized) efficiency can be achieved with a remarkably low loading amount of Pt SAs on TiO_2 nanosheets (0.03 wt%), which is far superior to Pt nanoparticles on TiO_2 nanosheet with the same or a higher loading amount. F-stabilized Pt SAs on TiO_2 nanosheets also exhibit an excellent stability in long-term photocatalytic reactions.

INTRODUCTION

Single-atom (SA) catalysts have drawn great attention in recent years owing to their excellent properties and applications in fields such as fuel cells, photocatalysis, and organic catalysis.[1-3] SA catalysts can realize a maximum atom-utilization efficiency and an outstanding catalytic performance owing to their spatial atomic isolation, distinct electronic structures and unsaturated coordination centers. Various strategies have been developed for the synthesis of SA catalysts, anchored in trapping sites with strong interactions to stabilize isolated atoms.[4-6] In this regard, a general method is to create suitable defect sites such as surface dislocations, oxo groups and vacancies to anchor the SAs.[7-10]

TiO_2 is the most widely investigated metal oxide semiconductor in photocatalysis due to its excellent stability and efficient photocatalytic activity. In photocatalytic H_2 production, TiO_2 needs to be decorated with a suitable co-catalyst such as Pt.[11-12] As such, TiO_2 has sufficient surface oxo groups for SA-trapping.[13-16] However, it is still challenging to stabilize many noble metals as SAs on TiO_2 surfaces

because of the relatively weak bonding between oxo groups and most noble metal SAs. That is to say, an enhanced interaction between metal SA and the substrate is desired to suppress agglomeration of SAs. In this context it can be conceived that the strong electronegativity of F could be exploited to stabilize SA cations. Fluorine, which has strong bonding to Ti (D_O^{F-Ti}=569.0 kJ mol^{-1}) and a similar atomic radius with oxygen,[17] can replace the oxygen atoms in TiO_2 without the distortion of its lattice structure and compromising its superior stability. Thus, doping F atoms into TiO_2 can theoretically improve the stability of anchored SAs by a strong adsorption of positive Pt ions and the enhanced Pt-F interaction.[18]

Over the last decades, TiO_2 nanosheets with high percentages of reactive (001) facets have been designed by fluorine based hydrothermal treatments.[19-21] These nanosheets usually have terminal F species absorbed on the surface and relatively stable F species doped in the lattice.[22, 23] Moreover, F species after nanosheet synthesis are present as unstable F species such as $TiOF_2$. In the present work, we investigate the effect of different F species on the stabilization of Pt SAs, manipulate the F speciation, and directly take advantage of the F species in TiO_2 nanosheets for a maximized stabilization and reactivity of Pt SAs for photocatalytic H_2 production. To condition the pristine fluorinated TiO_2 nanosheets (TiO_2-F), we first establish a well-defined NaOH treatment that selectively removes $TiOF_2$ and unstable terminal F species but retains stable lattice F species. The F species on TiO_2 nanosheets and their effect on the photocatalytic H_2 production were thoroughly investigated, clearly revealing the stabilization of Pt SAs by lattice F species. We show that such lattice F-stabilized Pt SAs provide a maximum efficiency with a minimum Pt SA loading. In fact, at a loading of only 0.03 wt% Pt is sufficient to achieve superior photocatalytic H_2 production efficiency. Based on the characterizations of F species and Pt SAs as well as the photocatalytic performance, a mechanism of fluorine aided stabilization of Pt single atoms is proposed.

RESULTS AND DISCUSSION

TiO_2 nanosheets were synthesized using a classic hydrothermal approach as described in the experimental section (SI). Then we exposed these sheets to various NaOH treatments and loaded the

samples (with and without NaOH treatment) with Pt SAs by a H_2PtCl_6 deposition approach described in the experimental section (SI).

Figure 1a shows the SEM and Figure 1c the high-angle annular dark field scanning transmission electron microscopy (HAADF-STEM) images for a non-NaOH-treated Pt SA loaded sample (Pt SAs/TiO_2-F), and Figure 1b and 1d the corresponding SEM and STEM images of an NaOH-treated sample (Pt SAs/TiO_2-OH_1).

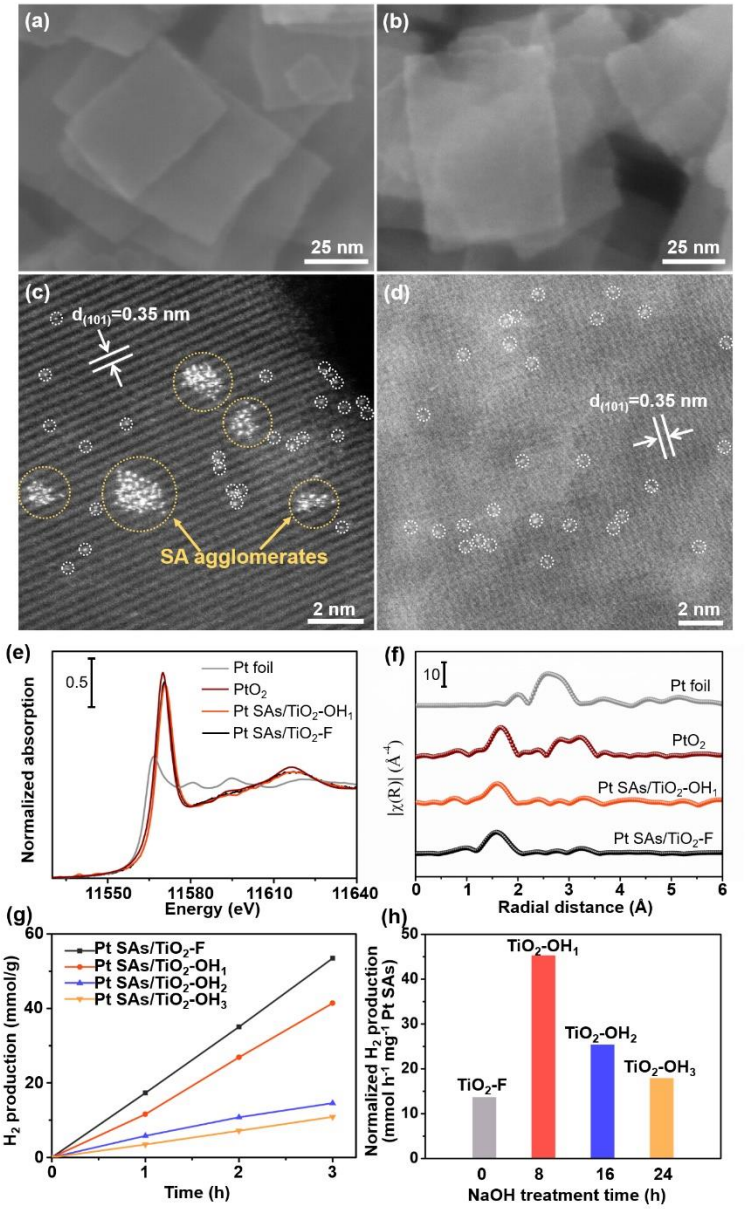

Figure 1. SEM images of a) Pt SAs/TiO_2-F, b) Pt SAs/TiO_2-OH_1; HAADF-STEM images of c) Pt SAs/TiO_2-F, d) Pt SAs/TiO_2-OH_1. e) Normalized XANES spectra at the Pt L_3 edge of Pt SAs/TiO_2-F and Pt SAs/TiO_2-OH_1. f) Fourier transform EXAFS spectra (R-space) of Pt SAs/TiO_2-F and Pt SAs/TiO_2-

OH_1. g) Photocatalytic H_2 evolution rate of Pt SAs on TiO_2 nanosheets with different NaOH treatment times. h) Normalized photocatalytic H_2 evolution rate of Pt SAs on TiO_2 nanosheet with different NaOH treatment time.

Before (TiO_2-F) and after the NaOH treatment (TiO_2-OH_1), the nanosheets show a typical near-square morphology with a square length of about 50 nm and a sheet thickness of some nanometers (Figure S1a, b). Also, after decoration with Pt, no noticeable change in morphology can be observed (Figure 1a, b). Notably, although a slight color change is observed after Pt deposition, no sign of Pt nanoclusters or nanoparticles can be observed on the surface of the nanosheets in SEM (Figure 1 a, b). X-ray diffraction (XRD) of both samples (Figure S2) show the diffraction patterns of anatase TiO_2 and no reflections associated with metallic Pt can be detected. However, clear differences between the TiO_2-F and TiO_2-OH_1 samples are evident from HAADF-STEM. The TiO_2-F surface shows well dispersed Pt SAs as well as some Pt SAs agglomerates on the surface of the nanosheets (Figure 1c). The EDXS mapping also indicates the existence of Pt SAs and SAs agglomerated on the TiO_2-F sheet (Figure S3a-c). In contrast, from the STEM image (Figure 1d) and EDXS mapping of TiO_2-OH_1 (Figure S3d-f), it can be observed that for the treated sheets the Pt SAs are very uniformly dispersed and no SAs agglomerates can be identified. X-ray absorption near-edge spectra (XANES) and X-ray absorption fine structure (EXAFS) measurements were further carried out to investigate the oxidation state of Pt and relevant atomic distances. The normalized XANES spectra measured at Pt L_3-edge (11.564 keV) suggests that all the samples bear positively charged Pt centers (Figure 1e).[24] The extended EXAFS analysis and the corresponding Fourier transformed radial distribution function (FT) shows a predominant feature at 1.6 Å (without phase correction) which originates from the Pt-O coordination (Figure 1f). This result indicates that the Pt is in highly dispersed state. From HAADF-TEM, an evaluation of density yields 1.25×10^6 Pt atoms/μm^2 for the TiO_2-F and 1.7×10^5 Pt atoms/μm^2 for the TiO_2-OH_1 surface (Figure S4), i.e., the TiO_2-F surface shows a significantly higher SAs loading than the TiO_2-OH_1 surface. Similar results can be obtained from STEM-EDXS, that shows TiO_2-F to carry a higher Pt loading amount (0.24

at%) than TiO_2-OH_1 (0.11 at%) (Table S1). Besides, TiO_2-F shows over 2-fold of F amount of TiO_2-OH_1 (1.34 at%) (Table S1), indicating the removal of surface F by the NaOH treatment. An average quantitative analysis of Pt using electrothermal atomization atomic absorption spectroscopy (ETA-AAS) analysis and SEM-EDX measurements (Table S2) shows that the NaOH treatment results in about a 2-5-fold decrease of the Pt loading amount of Pt SAs, but with extended NaOH treatment time no further decrease in the loading amount can be found. Figure 1g,h and Figure S5 show the photocatalytic H_2 evolution activity of the different SA decorated nanosheet samples. The photocatalytic H_2 evolution efficiency of Pt SA does not directly correlate with the decorated Pt SA amount. It is remarkable that while the TiO_2-F sheets show a slightly higher activity (17.6 mmol/g/h) than the TiO_2-OH sheets (which may be due to the significantly higher loading of atomic Pt), the mass specific activity (Figure 1h) is by far better for the TiO_2-OH sheet. I.e., although the Pt loading is reduced from 0.13 wt% to 0.03 wt% by the 8 h NaOH treatment, the H_2 generation activity hardly drops. Pt dark deposited on TiO_2 after NaOH treatment for 8 h shows the far highest mass specific photocatalytic efficiency (a H_2 production rate of 45.3 mmol h^{-1} per mg Pt SAs). This may be ascribed to ineffective SAs – recent work showed that more than 90 % of the Pt decorated as SAs not only does not contribute to the activity, but moreover such non-active Pt can be removed by cyanide leaching without an overall loss in H_2 evolution performance of the photocatalyst.[24] In any case, our present results show that a controlled NaOH treatment of TiO_2-F sheets affects the Pt loading amount and the averaged specific photocatalytic activity of the anchored SAs.

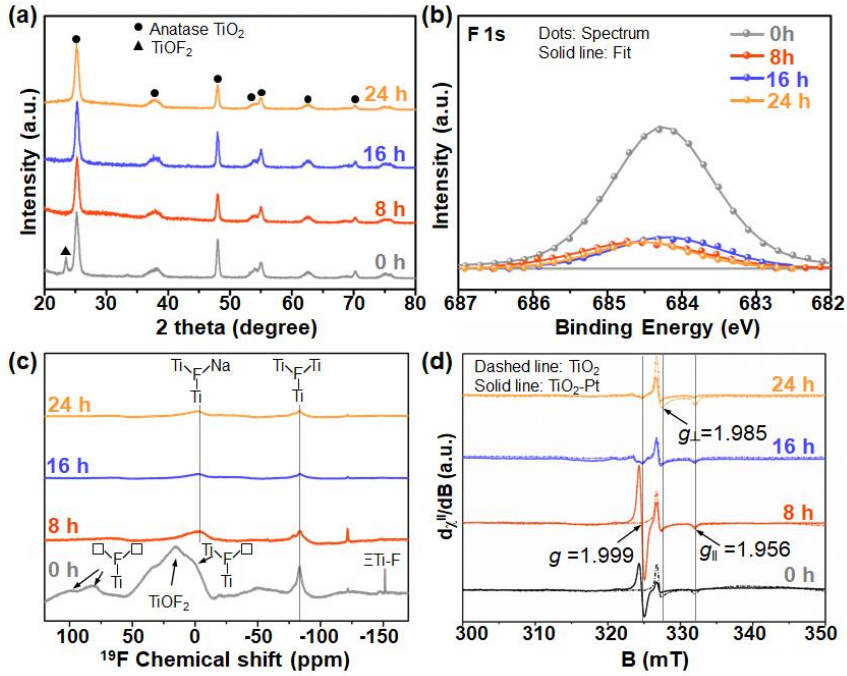

Figure 2. a) XRD patterns of TiO_2 nanosheets with different NaOH treatment times, b) XPS F 1s spectra of TiO_2 nanosheets treated with NaOH for different times, c) ^{19}F solid-state NMR spectra of TiO_2 nanosheets treated with NaOH for different times, d) EPR spectra of TiO_2 nanosheets treated with NaOH for different times and the treated TiO_2 with further deposition of Pt.

In order to reveal the effects of the NaOH treatment on TiO_2 nanosheets and at the same time to obtain information on the defect structure and the Pt coupling mechanism, we applied various techniques including XRD, Fourier transform infrared spectroscopy (FTIR), X-ray photoelectron spectroscopy (XPS), solid state nuclear magnetic resonance (NMR) and electron paramagnetic resonance (EPR). XRD patterns of the TiO_2-F show diffraction peaks of both anatase TiO_2 and of $TiOF_2$. The $TiOF_2$ phase disappears after NaOH treatment (Figure 2a), which indicates that $TiOF_2$ is unstable and could be removed. The FTIR spectrum of TiO_2-F (Figure S6) shows a broad band in the range of 3200-3500 cm^{-1} and a peak at 1635 cm^{-1} assigned to surface hydroxyl group (O-H).[25] In addition, it shows a broad band in the range of 900-1000 cm^{-1}, which can be assigned to Ti-F vibrations in $TiOF_2$.[26] This peak disappears after the NaOH treatment, confirming the successful removal of $TiOF_2$ in accordance with the XRD results. Moreover, after the NaOH treatment, a peak at 1330 cm^{-1} appears, which is attributed to the Ti-

OH group from the exchange of OH^- and F^- on the TiO_2 surface.[25] This means that overall loss of $TiOF_2$ and some surface Ti-F takes place. The XPS F 1s spectrum (Figure 2b) of TiO_2-F shows a peak with the binding energy of 684.7 eV, which is often found for F-terminated TiO_2 and $TiOF_2$ – however, differentiation of the species is difficult from XPS as there is hardly any peak separation between these species.[27, 28] After NaOH treatment for 8 h, it can be observed that the intensity of the F 1s peak is greatly decreased (Table S3). Notably, the amount of F^- shows no obvious decrease when longer time NaOH treatment is carried out. This, together with the XRD and FTIR findings, indicates that surface Ti-F is removed but still some stable F is present in/on TiO_2.

To further elucidate on the nature of this stable F species, ^{19}F solid-state NMR measurements were performed. As shown in Figure 2c, TiO_2-F show three main F species that have been previously assigned to Ti^{IV}□-F (100 and 80 ppm), Ti^{IV}□$_2$-F (~0 ppm) and Ti^{IV}_3-F (-80 ppm), respectively.[29] Besides, a strong NMR signal at ~15 ppm attributed to Ti_2-F from $TiOF_2$ and a sharp peak at -150 ppm attributed to surface terminal fluoride species $\equiv Ti - F$ indicate the existence of $TiOF_2$ and surface fluoride on TiO_2.[30, 31] (Note that the signal at -120 ppm is from the contamination of polytetrafluoroethylene). The results confirm that NaOH treatment can remove not only $TiOF_2$ but also some surface terminal fluoride species, and form Ti_2-F^-Na^+ (at -3 ppm) by the insertion of Na^+ in the Ti vacancy.[32] But evidently, Ti^{IV}_3-F present as a sub-surface species cannot be removed by NaOH treatment and also extended NaOH treatments have no obvious effect on Ti^{IV}_3-F. SEM images (Figure S1, Figure S7), Ti 2p and O 1s XPS spectra of the samples before and after NaOH treatment (Figure S8) show no obvious difference, which indicates that NaOH treatment has no influence on morphology and the surface composition. Based on the results above, it can be deduced that NaOH treatment is an effective way to remove unstable F species such as $TiOF_2$ and loose terminal fluoride on TiO_2 surface, but the stable F species in the TiO_2 lattice (or surface-near, sub-surface) are maintained.

From EPR, TiO_2-F (Figure 2d, black dashed trace) with the highest content of fluorine shows a weak axial signal with $g_\perp$=1.988 and $g_\parallel$=1.956, which are assigned to Ti^{3+} sites located in anatase TiO_2 phase.[33] This is due to the doping of F^- in O^{2-} lattice sites, which results in the reduction of Ti^{4+} to Ti^{3+} for charge

compensation.[34] Theoretical modelling further indicates that most of the spin is localized on the Ti(1) site (see Figure S9 in the supporting information) and this is the position that may preferentially interact with the Pt cation upon doping (*vide infra*) compared with the model that is F-free ($Ti_3O_{10}H_7$) (detailed description of the DFT calculations are given in the supporting information). NaOH treatment leads to the increase of the recorded EPR signal intensities matching with Ti^{3+} sites embedded in the lattice. Oxygen-based spin containing sites (e.g. Ti-O$^{\bullet}$), which show a signal that evolves typically around g=2.020 (320 mT), might be observed only as weak cluster resonances in samples treated in NaOH for 16 and 24 hours. [35, 36] Some surface exposed Ti^{3+} centres that usually express broad and unresolved signals around g=1.93 are also evident in our experiments.[36] After deposition of Pt SAs on the TiO_2 nanosheets, a decrease in the signal associated with lattice embedded Ti^{3+} sites can be observed (Figure 2d, solid trace), due to a galvanic displacement reaction ($Pt^{4+} \rightarrow Pt^{\delta+}$, $Ti^{3+} \rightarrow Ti^{4+}$, $\delta \approx 2$). The occurrence of such a process is supported by theory modelling where a spin transfer from Ti^{3+} site/s to the interacting Pt^{2+} cation occurs, this is accompanied by substantial reorganization of the S=1/2 spin distribution supported by oxygen and fluorine residues. Notably, another electron transfer process in TiO_2-F and NaOH-treated sample is apparent for the 8 h sample as well. More precisely, we observe the formation of a sharp isotropic signal positioned at g=1.999 (Figure 2d, black and red solid trace), which is associated to the generation of an electron trapped in an oxygen vacancy (V_O).[37] The generation of this signal may be attributed to the presence of a single Pt atom, which may induce the formation of V_O defects on the surface/subsurface.[38] Usually, V_O defects can provide a shallow donor level, that enhances electron transport, electrical conductivity and can improve the electrochemical reduction activities of the material.[39] Based on the EPR results and theoretical calculations, the Pt loading mechanism on TiO_2 nanosheets is proposed as: $F - Ti^{3+} + Pt^{4+} + O^{O} \rightarrow F - Ti^{4+} + Pt^{\delta+} + V_O^{\bullet} + (3-\delta)e'$ – thus reacting off surface-near EPR active lattice defects. Although the galvanic process appears to take place in TiO_2 system with Pt doping without the presence of F in the TiO_2 structure, it seems the galvanic displacement process is energetically favored in fluoride free titania but kinetically favored in F-containing titania.

The above results show that an appropriate NaOH treatment of the TiO_2 nanosheets can selectively remove unstable F species on the surface and while maintaining the strong interaction between Pt SAs and *stable* surface-near F species.

In the following, we compare the efficiencies of Pt SAs and Pt nanoparticles (NPs) on the NaOH-treated TiO_2 nanosheets, as well as the influence of different Pt loading amounts. Figure 3 a,b show the deconvoluted high resolution XPS spectra of the Pt 4f peak of Pt SAs/TiO_2 and TiO_2 decorated with Pt NPs (Pt NPs/TiO_2) produced by the synthesis procedure described in the supporting information. The Pt 4f peak of Pt SAs/TiO_2 can be fitted into two peaks at 72.4 eV and 75.7 eV (Figure 3a), which are attributed to $Pt^{\delta+}4f_{7/2}$ and $Pt^{\delta+}4f_{5/2}$, respectively.[40] This peak position can be regarded as evidence for presence of surface trapped Pt single atoms.[41] For comparison, the XPS peaks of Pt in the form of metallic nanoparticles show peak positions at 71.0 eV and 74.3 eV (Figure 3b) well in line with literature with metallic Pt^0.

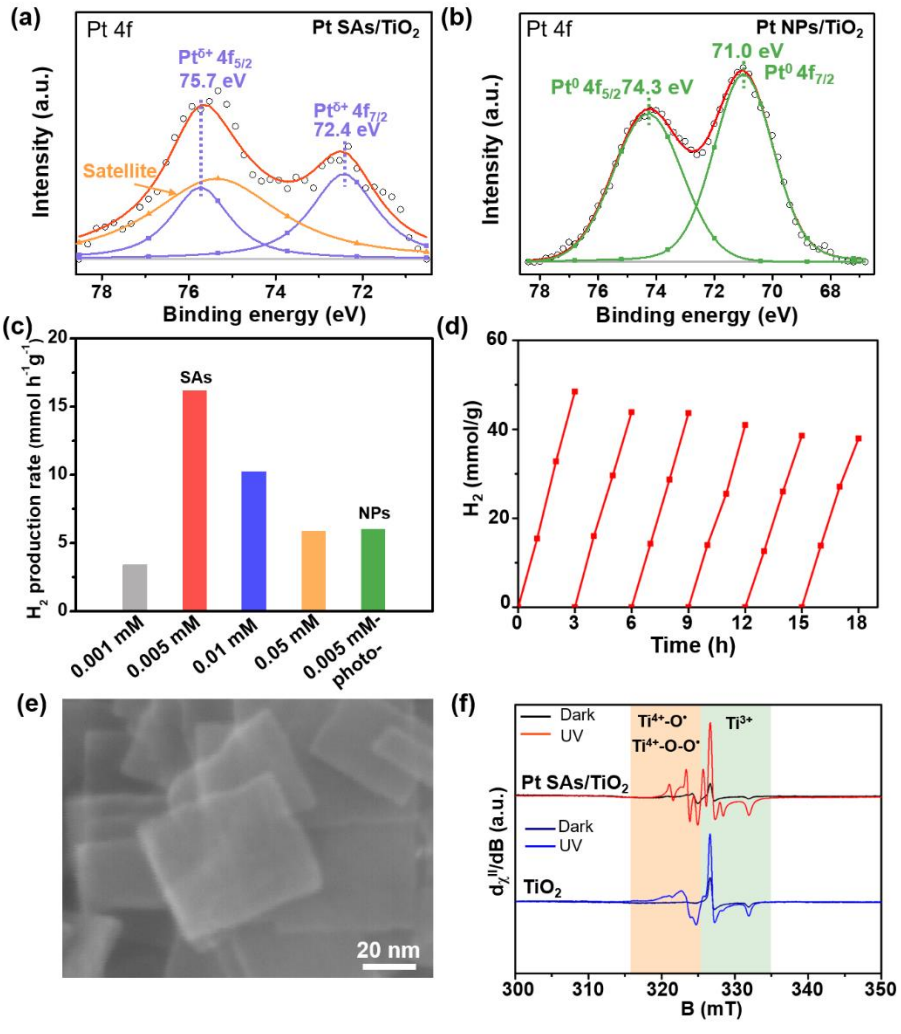

Figure 3. High-resolution XPS spectra of Pt 4f for: a) Pt SAs/TiO_2 and b) Pt NPs/TiO_2. c) Comparison of the hydrogen evolution rate over TiO_2 nanosheet deposited with different Pt concentration by different methods, d) Cycling measurements of photocatalytic hydrogen evolution over Pt SAs/TiO_2, e) SEM images of Pt SAs/TiO_2 after cycling measurements, f) X-band CW EPR spectra of TiO_2 and Pt SAs/TiO_2 dispersed in H_2O under dark condition and UV-irradiation (HeCd laser@325 nm, 200mW).

The influence of different concentrations of Pt-precursor (H_2PtCl_6) used for SA deposition is shown in Figure 3c, Figure S10 and Figure S11. Evidently, Pt SAs/TiO_2 synthesized with 0.005 mM H_2PtCl_6 shows the highest H_2 evolution rate compared with other samples. Increasing the Pt loading up to deposition from 0.005 mM Pt solution increases the photocatalytic activity, but a further increase of the Pt amount leads to the formation of Pt agglomerates or nanoparticles which can be observed in SEM images (Figure S12). Also evident is that in spite of a much higher Pt loading for the Pt agglomerates (Table S4), the photocatalytic activity is lower compared to SA Pt. Besides, also nanoparticles formed by conventional photodeposition with a similar loading amount of Pt (Figure S12g,h, Table S4) also shows a lower photocatalytic H_2 performance than Pt SAs. This emphasizes the high efficiency of Pt deposited in the form of single atoms on the NaOH-treated F-TiO_2.

Moreover, the Pt SAs/TiO_2 sample shows a remarkable long-term stability. In long-term photocatalytic H_2 experiments (Figure 3d), over 80% of the photocatalytic activity is maintained after 6 cycles (18 h) of H_2 production, which reflects the great stability of Pt SAs on TiO_2. Please note that extended illumination leads for "loosely bound Pt" on the TiO_2-F sheets to an agglomeration that is visible in SEM (Figure S13) while for the TiO_2-OH sample (Figure 3e, Figure S14) no change compared with the sample before illumination and no Pt particles can be observed on the surface of TiO_2. From XANES spectra at the Pt L_3-edge, it can be observed that after UV irradiation, the white line intensity significantly decreases meaning that TiO_2-F-Pt-UV forms some Pt clusters, but for theTiO_2-OH_1-Pt-UV only a small fraction of reduced Pt species remains (Figure S15a). Fourier transformed EXAFS spectra also show that TiO_2-F-Pt-UV sample form Pt clusters as Pt-Pt interaction can be observed at a radial distance of 2.6 Å (without

phase correction). However, the OH-treated TiO_2-OH_1-Pt-UV shows the co-existence of Pt-O and Pt-Pt upon UV irradiation (Figure S15b). HAADF-STEM image (Figure S16) also clearly shows the existence of Pt SAs in TiO_2-OH_1-Pt-UV. These results clearly reflect the higher stability of Pt SAs in TiO_2-OH_1-Pt than in TiO_2-F-Pt.

To gain further insights into the photogenerated carriers under H_2 production conditions, the EPR spectra of TiO_2-OH_1 and Pt SAs/TiO_2-OH_1 were also measured under irradiation with a HeCd (325 nm) laser. TiO_2 show an increase of the axial signal ($g_\perp$=1.988; $g_\parallel$=1.958) associated to the Ti^{3+} sites and at the same time formation of fingerprints of photoexcited holes, exhibiting rhombic signal at g_x= 2.025; g_y=2.011 and g_z=2.005 (Figure 3f). While Ti^{3+} sharp resonant line points towards location of the spin in the crystal lattice, oxygen-based holes show significantly larger line width and therefore these species are located on, or close to, the nanoparticle surface. The presence of Pt SAs on the titania (Figure 3f) significantly changes the nature of photoexcited species. Notably, Ti-$O^\bullet$ holes show a substantial decrease in linewidth, an indication of their localization onto confined sites, possibly in subsurface regions. Moreover, these sharp signals associated to the photoexcited hole centres indicate that the magnetic dipolar interactions with neighbouring spin-effective systems are weakened in Pt SAs compared to neat TiO_2, an effect that may point towards to the less proclivity of h^+ in Pt SAs to fast recombine with photoexcited e^- compared to neat TiO_2. As for the case of Ti^{3+} sites, besides the signal increase at $g_\perp$=1.988; $g_\parallel$=1.958, it is noticed the formation upon photoexcitation of a cluster of new resonances at $g_\perp$=1.994 and $g_\parallel$=1.979, hence characterized by rather small *g*-anisotropy. In this context, it is important to note that the dominant character of the spin wavefunction associated to the above g-tensor remain dominated by the Ti^{3+} 3d-orbitals, because the effective *g*-value (g-eff = 1.989) is still smaller than the free electron in the vacuum, due to the positive term of the spin-orbit coupling constant (SOC) of Ti^{3+} (~155 cm^{-1}). However, a close proximity of such Ti^{3+} centres to $Pt^{\delta+}$ sites (5d orbitals, $Pt^{+/2+}$ has large negative SOC) located onto neighbouring Vo to Ti^{3+} can promote an electronic reorganization of the photoexcited spin system,[42] adopting the form of F-Ti^{3+}/ $Pt^{\delta+}$ ↔ F-Ti^{4+}/$Pt^{\delta-1}$, which leads to the observed reduction in *g*-tensor anisotropy as shown earlier in the model $PtTi_3O_8F_2H_7$ (Figure S9b).

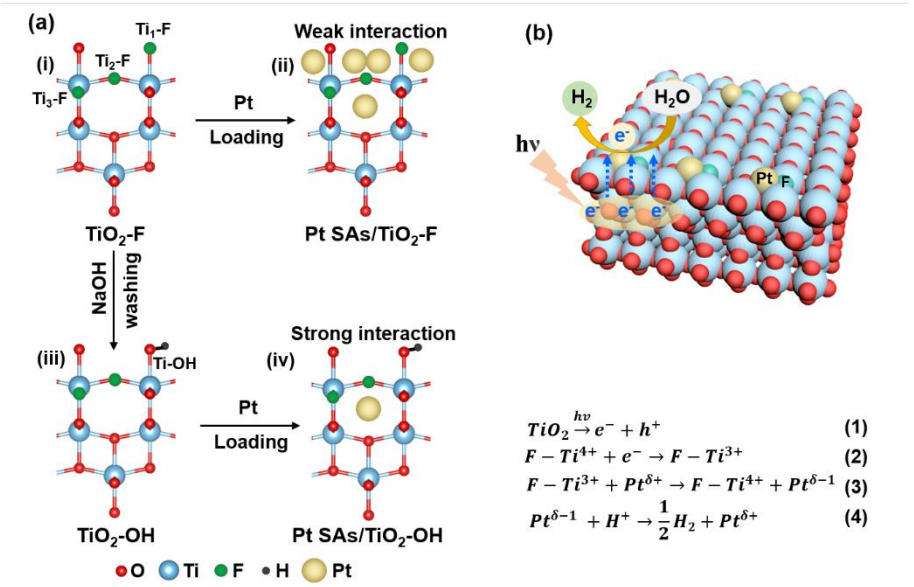

Figure 4. a) Proposed formation mechanism of Pt SAs/TiO_2, structure model of i) as prepared TiO_2 nanosheets (TiO_2-F) with different F species (surface F: Ti_1-F, lattice F: Ti_2-F and Ti_3-F), ii) after Pt SAs deposition on TiO_2-F, iii) NaOH treated TiO_2 nanosheets (TiO_2-OH) without Ti_1-F, iv) after Pt SAs deposition on TiO_2-OH, b) Structure models and schematic illustration of charge transfer process in Pt SAs/TiO_2-OH.

Based on above results, a possible mechanism for the beneficial interaction of SA Pt and F in/on TiO_2 nanosheet can be proposed. In pristine TiO_2-F nanosheets, there are surface terminal F species (Figure 4a, i), which can generate both surface and lattice Ti^{3+} suitable for Pt anchoring and charge compensation (Figure 4a, ii).[43] For the non-NaOH treated samples, due to the high level of F-termination, a high loading of weakly bound SA Pt can take place. This high Pt loading for TiO_2-F samples is verified by AAS (Table S2). However, these loosely bound Pt SAs tend to easily agglomerate on the surface to rafts, as shown in the STEM images (Figure 1c). These Pt agglomerates have weak interaction with the surface and can easily further aggregate under illumination (Figure S13). Moreover, this loosely bound Pt hardly contributes to the overall co-catalytic activity of the Pt decoration. The NaOH treatment removes the surface F species and only the stable lattice F species remain (Figure 4a, iii). Pt SAs interacting with such F-induced unsaturated sites are stabilized (Figure 4a, iv) and photoelectrons would then be able to transfer to these stabilized Pt atoms for H_2 production (Figure 4b). In general, F species, due to the high

electronegativity, are beneficial for charge compensation,[44] i.e. aid trapping of positively charged Pt SAs and thus promote the transfer of photoelectrons to the anchored $Pt^{\delta+}$ for H_2 evolution. While this role could be played by surface and sub-surface F, the present work shows clearly that the key effect is the strong co-catalytic effect of lattice F-stabilized Pt SAs where hardly any catalytic activity loss over time and only limited SA agglomeration can be observed (Figure S11, Figure S15).

CONCLUSIONS

In the present work we place single atom Pt species onto hydrothermally synthesized TiO_2 anatase nanosheets. The use of a fluoride capping agent in the hydrothermal synthesis leads to different fluoride species on the nanosheets (F-surface terminated) and (subsurface) in the lattice of the nanosheets. The F-species aid the loading and anchoring of Pt as SAs in- and on the nanosheets. Adjusted NaOH treatments can selectively remove loosely-bound surface-F, whereas sub-surface lattice F remains stable. Bound F-species induce Ti^{3+} states that are able to trap Pt-SAs and anchor them in a stable configuration. Overall, a suitable treatment of F-TiO_2 with NaOH leads to a low density of Pt SAs on TiO_2 ($\approx 1.7\times10^5$ /μm^2) – these SAs however are stable against agglomeration and provide the maximum photocatalytic H_2 evolution efficiency with 45.3 mmol $h^{-1}mg^{-1}_{(Pt)}$. A higher Pt loading leads to loosely attached (weakly adsorbed surface Pt SAs) that easily agglomerate and do not significantly contribute to the overall co-catalytic effect of Pt. This work thus provides an effective method for the design of high-performance single atom photocatalyst using the interaction of stable F in TiO_2 nanosheets that in turn aids the stabilization of Pt SAs and to an excellent photocatalytic stability.

ASSOCIATED CONTENT

AUTHOR INFORMATION

Corresponding Author

*Email: schmuki@ww.uni-erlangen.de

Author Contributions

The manuscript was written through contributions of all authors. All authors have given approval to the final version of the manuscript.

Notes

The authors declare no competing financial interest.

Supporting Information.

This information is available free of charge on the ACS Publications website.

Experimental section; SEM and TEM images, XRD patterns, FT-IR spectra, XPS spectra, XANES, Pt loading amount measurements (XPS, SEM-EDX, STEM-EDXS, AAS), and comparison of photocatalytic activity.

ACKNOWLEDGMENT

The authors would like to acknowledge the DFG and the Operational research program, Development and Education (European Regional Development Fund, Project No. CZ.02.1.01/0.0/0.0/15_003/0000416 of the Ministry of Education, Youth and Sports of the Czech Republic) for financial support. S. W. thanks the Alexander von Humboldt Foundation, Bonn, Germany, for funding the postdoctoral fellowship. Jan Kolarik is greatly appreciated for his help with quantitative determination using atomic absorption spectroscopy. We would like to thank Dr. Edmund Welter, beamline scientist, P65, PETRA III, DESY, Hamburg and Dr. Dmitry Doronkin, KIT for their help in setting up the beamline.

REFERENCES

1. Kaiser, S. K.; Chen, Z.; Faust Akl, D.; Mitchell, S.; Pérez-Ramírez, J., Single-Atom Catalysts across the Periodic Table. *Chem. Rev.* **2020**, *120*, 11703-11809.

2. Gao, C.; Low, J.; Long, R.; Kong, T.; Zhu, J.; Xiong, Y., Heterogeneous Single-Atom Photocatalysts: Fundamentals and Applications. *Chem. Rev.* **2020,** *120*, 12175-12216.

3. Yang, X.-F.; Wang, A.; Qiao, B.; Li, J.; Liu, J.; Zhang, T., Single-Atom Catalysts: A New Frontier in Heterogeneous Catalysis. *Acc. Chem. Res.* **2013**, *46*, 1740-1748.

4. Chen, Y.; Ji, S.; Chen, C.; Peng, Q.; Wang, D.; Li, Y., Single-Atom Catalysts: Synthetic Strategies and Electrochemical Applications. *Joule* **2018**, *2*, 1242-1264.

5. Xi, J.; Jung, H. S.; Xu, Y.; Xiao, F.; Bae, J. W.; Wang, S., Synthesis Strategies, Catalytic Applications, and Performance Regulation of Single-Atom Catalysts. *Adv. Funct. Mater.* **2021**, *31*, 2008318.

6. Liu, K.; Zhao, X.; Ren, G.; Yang, T.; Ren, Y.; Lee, A. F.; Su, Y.; Pan, X.; Zhang, J.; Chen, Z.; Yang, J.; Liu, X.; Zhou, T.; Xi, W.; Luo, J.; Zeng, C.; Matsumoto, H.; Liu, W.; Jiang, Q.; Wilson, K.; Wang, A.; Qiao, B.; Li, W.; Zhang, T., Strong Metal-support Interaction Promoted Scalable Production of Thermally Stable Single-atom Catalysts. *Nat. Commun.* **2020**, *11*, 1263.

7. Wu, Z.; Hwang, I.; Cha, G.; Qin, S.; Tomanec, O.; Badura, Z.; Kment, S.; Zboril, R.; Schmuki, P., Optimized Pt Single Atom Harvesting on TiO_2 Nanotubes—Towards a Most Efficient Photocatalyst. *Small* **2022**, *18*, 2104892.

8. Qiao, B.; Wang, A.; Yang, X.; Allard, L. F.; Jiang, Z.; Cui, Y.; Liu, J.; Li, J.; Zhang, T., Single-atom Catalysis of CO Oxidation Using Pt_1/FeO_x. *Nat. Chem.* **2011**, *3*, 634-641.

9. Zhang, L.; Zhao, X.; Yuan, Z.; Wu, M.; Zhou, H., Oxygen Defect-stabilized Heterogeneous Single Atom Catalysts: Preparation, Properties and Catalytic Application. *J. Mater. Chem. A* **2021**, *9*, 3855-3879.

10. Cha, G.; Mazare, A.; Hwang, I.; Denisov, N.; Will, J.; Yokosawa, T.; Badura, Z.; Zoppellaro, G.; Tesler, A. B.; Spiecker, E.; Schmuki, P., A Facile “dark”-deposition Approach for Pt Single‐atom Trapping on Facetted Anatase TiO_2 Nanoflakes and Use in Photocatalytic H_2 Generation. *Electrochim. Acta* **2022**, *412*, 140129.

11. Hejazi, S. M. H.; Shahrezaei, M.; Błoński, P.; Allieta, M.; Sheverdyaeva, P. M.; Moras, P.; Baďura, Z.; Kalytchuk, S.; Mohammadi, E.; Zbořil, R.; Kment, Š.; Otyepka, M.; Naldoni, A.; Fornasiero, P., Defect Engineering Over Anisotropic Brookite Toward Substrate-Specific Photo-Oxidation of Alcohols, *Chem Catal.* **2022**, *2*, 1177-1190.

12. Hwang, I.; Mazare, A.; Will, J.; Yokosawa, T.; Spiecker, E.; Schmuki, P., Inhibition of H_2 and O_2 Recombination: The Key to a Most Efficient Single-Atom Co-Catalyst for Photocatalytic H_2 Evolution from Plain Water. *Adv. Funct. Mater.* **2022,** *32*, 2207849.

13. Thompson, T. L.; Yates, J. T., Surface Science Studies of the Photoactivation of TiO_2 New Photochemical Processes. *Chem. Rev.* **2006**, *106*, 4428-4453.

14. Kerketta, U.; Tesler, A. B.; Schmuki, P., Single-Atom Co-Catalysts Employed in Titanium Dioxide Photocatalysis. *Catalysts* **2022**, *12*, 1223.

15. Xiao, S.-T.; Wu, S.-M.; Dong, Y.; Liu, J.-W.; Wang, L.-Y.; Wu, L.; Zhang, Y.-X.; Tian, G.; Janiak, C.; Shalom, M., Rich surface hydroxyl design for nanostructured TiO_2 and its hole-trapping effect. *Chem. Eng. J.* **2020**, *400*, 125909.

16. Zhou, X.; Hwang, I.; Tomanec, O.; Fehn, D.; Mazare, A.; Zboril, R.; Meyer, K.; Schmuki, P., Advanced Photocatalysts: Pinning Single Atom Co-Catalysts on Titania Nanotubes. *Adv. Funct. Mater.* **2021**, *31*, 2102843.

17. Luo, Y.-R., *Comprehensive handbook of chemical bond energies*. CRC press: Boca Raton, FL, **2007**, 14, p 1-22.

18. Ji, W.; Wang, X.; Tang, M.; Yang, L.; Rui, Z.; Tong, Y.; Lin, J. Y. S., Strategy for Stabilizing Noble Metal Nanoparticles without Sacrificing Active Sites. *Chem. Commun.* **2019**, *55*, 6846-6849.

19. Han, X.; Kuang, Q.; Jin, M.; Xie, Z.; Zheng, L., Synthesis of Titania Nanosheets with a High Percentage of Exposed (001) Facets and Related Photocatalytic Properties. *J. Am. Chem. Soc.* **2009**, *131*, 3152-3153.

20. Liu, S.; Yu, J.; Jaroniec, M., Anatase TiO_2 with Dominant High-Energy {001} Facets: Synthesis, Properties, and Applications. *Chem. Mater.* **2011**, *23*, 4085-4093.

21. Sajan, C. P.; Wageh, S.; Al-Ghamdi, A. A.; Yu, J.; Cao, S., TiO_2 nanosheets with Exposed {001} Facets for Photocatalytic Applications. *Nano Res.* **2016**, *9*, 3-27.

22. Pellegrino, F.; Morra, E.; Mino, L.; Martra, G.; Chiesa, M.; Maurino, V., Surface and Bulk Distribution of Fluorides and Ti^{3+} Species in TiO_2 Nanosheets: Implications on Charge Carrier Dynamics and Photocatalysis. *J. Phys. Chem. C* **2020**, *124*, 3141-3149.

23. Zhang, Y.; Shang, M.; Mi, Y.; Xia, T.; Wallenmeyer, P.; Murowchick, J.; Dong, L.; Zhang, Q.; Chen, X., Influence of the Amount of Hydrogen Fluoride on the Formation of (001)-Faceted Titanium Dioxide Nanosheets and Their Photocatalytic Hydrogen Generation Performance. *ChemPlusChem* **2014**, *79*, 1159-1166.

24. Qin, S.; Denisov, N.; Will, J.; Kolařík, J.; Spiecker, E.; Schmuki, P., A Few Pt Single Atoms Are Responsible for the Overall Co-Catalytic Activity in Pt/TiO_2 Photocatalytic H_2 Generation. *Solar RRL* **2022**, *6*, 2101026.

25. Subalakshmi, K.; Senthilselvan, J., Effect of Fluorine-doped TiO_2 Photoanode on Electron Transport, Recombination Dynamics and Improved DSSC Efficiency. *Solar Energy* **2018**, *171*, 914-928.

26. Zhang, Y.; Zhang, Q.; Xia, T.; Zhu, D.; Chen, Y.; Chen, X., The Influence of Reaction Temperature on the Formation and Photocatalytic Hydrogen Generation of (001) Faceted TiO_2 Nanosheets. *ChemNanoMat* **2015**, *1*, 270-275.

27. Yu, J. C.; Yu; Ho; Jiang; Zhang, Effects of F- Doping on the Photocatalytic Activity and Microstructures of Nanocrystalline TiO_2 Powders. *Chem. Mater.* **2002**, *14*, 3808-3816.

28. Huang, Z. A.; Wang, Z.; Lv, K.; Zheng, Y.; Deng, K., Transformation of $TiOF_2$ Cube to a Hollow Nanobox Assembly from Anatase TiO_2 Nanosheets with Exposed {001} Facets via Solvothermal Strategy. *ACS Appl. Mater. Interfaces* **2013**, *5*, 8663-8669.

29. Koketsu, T.; Ma, J.; Morgan, B. J.; Body, M.; Legein, C.; Dachraoui, W.; Giannini, M.; Demortière, A.; Salanne, M.; Dardoize, F.; Groult, H.; Borkiewicz, O. J.; Chapman, K. W.; Strasser, P.; Dambournet, D., Reversible Magnesium and Aluminium Ions Insertion in Cation-deficient Anatase TiO_2. *Nat. Mater.* **2017,** *16*, 1142-1148.

30. Serre, C.; Corbière, T.; Lorentz, C.; Taulelle, F.; Férey, G., Hydrothermal Synthesis of Nanoporous Metalofluorophosphates. 1. Precursor Solutions of Titanium Fluoride and Fluorophosphate in Water, a ^{19}F and ^{31}P NMR Study. *Chem. Mater.* **2002**, *14*, 4939-4947.

31. Hu, J.; Lu, Y.; Liu, X.-L.; Janiak, C.; Geng, W.; Wu, S.-M.; Zhao, X.-F.; Wang, L.-Y.; Tian, G.; Zhang, Y.; Su, B.-L.; Yang, X.-Y., Photoinduced Terminal Fluorine and Ti^{3+} in $TiOF_2/TiO_2$ Heterostructure for Enhanced Charge Transfer. *CCS Chem.* **2020**, *2*, 1573-1581.

32. Ruan, L.; Wang, X.; Wang, T.; Ren, Z.; Chen, Y.; Zhao, R.; Zhou, D.; Fu, G.; Li, S.; Gao, L.; Lu, Y.; Wang, Z.; Tian, H.; Kong, X.; Han, G., Surface Defect-Controlled Growth and High Photocatalytic H_2 Production Efficiency of Anatase TiO_2 Nanosheets. *ACS Appl. Mater. Interfaces* **2019**, *11*, 37256-37262.

33. Livraghi, S.; Chiesa, M.; Paganini, M. C.; Giamello, E., On the Nature of Reduced States in Titanium Dioxide As Monitored by Electron Paramagnetic Resonance. I: The Anatase Case. *J. Phys. Chem. C* **2011**, *115*, 25413-25421.

34. Czoska, A. M.; Livraghi, S.; Chiesa, M.; Giamello, E.; Agnoli, S.; Granozzi, G.; Finazzi, E.; Valentin, C. D.; Pacchioni, G., The Nature of Defects in Fluorine-Doped TiO_2. *J. Phys. Chem. C* **2008**, *112*, 8951-8956.

35. Sekiya, T.; Takeda, H.; Kamiya, N.; Kurita, S.; Kodaira, T., EPR of Anatase Titanium Dioxide Under UV Light Irradiation. *Phys. Status Solidi C* **2006**, *3*, 3603-3606.

36. Naldoni, A.; Altomare, M.; Zoppellaro, G.; Liu, N.; Kment, Š.; Zbořil, R.; Schmuki, P., Photocatalysis with Reduced TiO_2: From Black TiO_2 to Cocatalyst-Free Hydrogen Production. *ACS Catal.* **2019**, *9*, 345-364.

37. Wu, S. M.; Liu, X. L.; Lian, X. L.; Tian, G.; Janiak, C.; Zhang, Y. X.; Lu, Y.; Yu, H. Z.; Hu, J.; Wei, H., Homojunction of Oxygen and Titanium Vacancies and Its Interfacial n–p Effect. *Adv. Mater.* **2018**, *30*, 1802173.

38. Cai, S.; Wang, L.; Heng, S.; Li, H.; Bai, Y.; Dang, D.; Wang, Q.; Zhang, P.; He, C., Interaction of Single-Atom Platinum–Oxygen Vacancy Defects for the Boosted Photosplitting Water H_2 Evolution and CO_2 Photoreduction: Experimental and Theoretical Study. *J. Phys. Chem. C* **2020**, *124*, 24566-24579.

39. Bad'ura, Z.; Naldoni, A.; Qin, S.; Bakandritsos, A.; Kment, Š.; Schmuki, P.; Zoppellaro, G., Light-Induced Migration of Spin Defects in TiO_2 Nanosystems and their Contribution to the H_2 Evolution Catalysis from Water. *ChemSusChem* **2021**, *14*, 4408-4414.

40. Hejazi, S.; Mohajernia, S.; Osuagwu, B.; Zoppellaro, G.; Andryskova, P.; Tomanec, O.; Kment, S.; Zbořil, R.; Schmuki, P., On the Controlled Loading of Single Platinum Atoms as a Co-Catalyst on TiO_2 Anatase for Optimized Photocatalytic H_2 Generation. *Adv.Mater.* **2020**, *32*, 1908505.

41. Daelman, N.; Capdevila-Cortada, M.; López, N., Dynamic Charge and Oxidation State of Pt/CeO_2 Single-atom Catalysts. *Nat. Mater.* **2019**, *18*, 1215-1221.

42. Koseki, S.; Matsunaga, N.; Asada, T.; Schmidt, M. W.; Gordon, M. S., Spin–Orbit Coupling Constants in Atoms and Ions of Transition Elements: Comparison of Effective Core Potentials, Model Core Potentials, and All-Electron Methods. *J. Phys. Chem. A* **2019**, *123*, 2325-2339.

43. Chen, Y.; Ji, S.; Sun, W.; Lei, Y.; Wang, Q.; Li, A.; Chen, W.; Zhou, G.; Zhang, Z.; Wang, Y.; Zheng, L.; Zhang, Q.; Gu, L.; Han, X.; Wang, D.; Li, Y., Engineering the Atomic Interface with Single Platinum Atoms for Enhanced Photocatalytic Hydrogen Production. *Angew. Chem. Int. Ed.* **2020**, *59*, 1295-1301.

44. Park, H.; Choi, W., Effects of TiO_2 Surface Fluorination on Photocatalytic Reactions and Photoelectrochemical Behaviors. *J. Phys. Chem. B* **2004**, *108*, 4086-4093.

Supporting Information

Fluorine Aided Stabilization of Pt Single Atoms on TiO_2 Nanosheets and Strongly Enhanced Photocatalytic H_2 Evolution

Si-Ming Wu,[†] Imgon Hwang,[†] Benedict Osuagwu,[†] Johannes Will,[‡] Zhenni Wu,[†] Bidyut Bikash Sarma,[‖] Fu-Fei Pu,[+] Li-Ying Wang,[§] Zdenek Badura,[Δ] Giorgio Zoppellaro,[Δ] Erdmann Spiecker,[‡] and Patrik Schmuki[*†Δ±]*

[†]Department of Materials Science WW4-LKO, University of Erlangen-Nuremberg, Martensstraße 7, 91058 Erlangen, Germany

[‡]Institute of Micro- and Nanostructure Research & Center for Nanoanalysis and Electron Microscopy (CENEM), University of Erlangen-Nuremberg, IZNF, Cauerstraße 3, 91058 Erlangen, Germany

[‖]Institute of Catalysis Research and Technology (IKFT) and Institute for Chemical Technology and Polymer Chemistry (ITCP), Karlsruhe Institute of Technology (KIT), Hermann-von-Helmholtz-Platz 1, 76344 Eggenstein-Leopoldshafen, Germany

[+]School of Materials Science and Engineering, Wuhan University of Technology, Wuhan, 430070, China.

[§]State Key Laboratory of Magnetic Resonance and Atomic and Molecular Physics, Wuhan Institute of Physics and Mathematics, The Chinese Academy of Sciences, Wuhan, 430071, China

[Δ]Regional Centre of Advanced Technologies and Materials, Šlechtitelů 27, Olomouc 78371, Czech Republic

[±]Department of Chemistry, Faculty of Science, King Abdulaziz University, P.O. Box 80203, Jeddah 21569, Saudi Arabia

*Corresponding Author: schmuki@ww.uni-erlangen.de

Experimental Section

Synthesis

Synthesis of pristine TiO_2 nanosheets (TiO_2-F): TiO_2 nanosheets were synthesized by a hydrothermal method. Typically, 1.2 mL of concentrated hydrofluoric acid (HF, 48%) was added dropwise to 10 mL of tetrabutyl titanate ($Ti(OBu)_4$) under stirring. After 40 min, the mixture was sealed in a Teflon autoclave and transferred to a preheated oven at 200 °C. After hydrothermal reaction for 24 h and cooling, the precipitates were collected, washed with acetone and distilled water several times, and finally dried in an oven at 75 °C overnight.

NaOH treatment of the TiO_2 nanosheets (TiO_2-OH_x): The obtained powder was dispersed in 0.1 M NaOH and stirred for 8 h, 16 h, 24 h to partially remove the fluorides on the surface. The products were collected by centrifugation, washed with distilled water several times, and then dried at 75 °C overnight. The samples with 8 h, 16 h, 24 h NaOH treatment were named as TiO_2-OH_1, TiO_2-OH_2, TiO_2-OH_3, respectively.

Dark deposition of Pt on TiO_2 nanosheets: 40 mg of TiO_2 were added into 100 mL of the $H_2PtCl_6 \cdot 6H_2O$ aqueous solution with different concentrations under stirring. The solution was then purged with Ar for 30 mins to remove residual gases, such as oxygen and nitrogen. The container was then sealed and stirred in dark environment for 24 h. The sample dark deposited with 0.005 mM $H_2PtCl_6 \cdot 6H_2O$ was designated as Pt

SAs/TiO_2, and the sample dark deposited with 0.05 mM $H_2PtCl_6 \cdot 6H_2O$ was designated as Pt NPs/TiO_2.

Photodeposition of Pt on TiO_2 nanosheets: A reference sample was decorated with Pt nanoparticles by photodeposition. For this, 40 mg of TiO_2 were added into 100 mL of the $H_2PtCl_6 \cdot 6H_2O$ aqueous solution under stirring. The reactor was then illuminated for 20 h with an AM 1.5G light source. The products were collected by high-speed centrifugation, washed with distilled water for several times, and then dried at 75 °C overnight.

Characterization

The morphology of the samples was investigated with a field-emission scanning electron microscope (FE-SEM) Hitachi FE-SEM 4800. X-ray photoelectron spectroscopy (XPS, PHI 5600, US) was used to investigate the surface property of the samples. Accurate binding energies were determined with respect to the position of the adventitious C 1s peak at 284.8 eV. X-ray diffraction analysis (XRD) was conducted with an X'pert Philips MPD (with a Panalytical X'celerator detector) using graphite monochromized Cu Ka radiation (λ= 1.54056 A˚).

Atomically resolved structural characterization was performed by a Thermo Fisher Scientific Spectra 200 C-FEG transmission electron microscope. The probe corrected instrument is equipped with an ultra-high-brightness cold field emission gun (X-CFEG) and a high-sensitivity SDD X-ray spectrometer (Super-X) for energy-dispersive X-ray

spectroscopy (EDXS). For high-angle annular dark field imaging of Pt SAs on TiO_2, an acceleration voltage of 200 kV in combination with dwell times from 5 to 20 µs, beam currents below 30 pA, and an collection angle ranging from 56 to 200 mrad was chosen.

EPR spectra were collected on X-band (~9.14-9.17 GHz) spectrometer JEOL JES-X-320 equipped by variable He temperature set-up ES-CT470 apparatus. Experimental temperature was set to 80 K. The quality factor (Q) was kept above 6000 for all measurements to make the spectra comparable. As a sample holder high purity quartz tubes (Suprasil, Wilmad, ≤0.5 OD) were used, and the accuracy of the g-values was determined by comparison with a $Mn^{2+/}$MgO standard (JEOL standard). The microwave power was set to 2.0 mW to avoid any power saturation effects. A modulation width of 0.5 mT and a modulation frequency of 100 kHz were used. All EPR spectra were collected with a time constant of 30 ms and a sweep time of 2 min with three accumulations to improve the signal-to-noise ratio. The loading amount of Pt was also determined by atomic absorption spectroscopy (AAS) with electrothermal atomization (AAS-ETA) using a graphite furnace with a ContrAA 600 Spectrometer (Analytik Jena AG) equipped with a high-resolution Echelle double monochromator and with a continuum radiation source (Xe lamp). Fourier-transform infrared (FT-IR) spectra were obtained with a Jasco FT/IR-4700 spectrometer. ^{19}F MAS NMR measurement was carried out in a 2.5 mm MAS probe on a Bruker AVANCE-III 500 spectrometer with a sample spinning rate of 30 kHz, a ^{19}F $\pi/2$ pulse length of 1.75 us and a recycle delay of 1 s.

The X-ray absorption were carried out at Pt L_3-edge (11.564 keV) and a Si(111) double crystal monochromator was used to scan the incident energy. The energy was calibrated with a reference metal foil. All the spectra were collected at P65 (Petra III) beamline at the Deutsches Elektronen-Synchrotron (DESY) Hamburg, Germany. The measurements were conducted in transmission mode (for PtO_2 reference diluted with cellulose and pressed in a pellet) and the catalysts were measured in fluorescence mode (in a quartz capillary pressed between quartz wool without any dilution). A Ge detector was used to collect the fluorescence X-rays. XAS data reduction was carried out using the standard Demeter software packages. Data reduction (alignment and normalization) was performed using the Athena code (version 0.9.26).

Photocatalytic H_2 evolution experiments

2 mg of the catalyst was added into 10 mL 50 vol% MeOH solution in a quartz reactor. After sonication for 1 min and purging with Ar for 15 min, the reactor was sealed and then irradiated with a 365 nm LED (power intensity: 65 mW cm^{-2}) under stirring. Evolved H_2 was determined by a gas chromatograph (GCMS-QO2010SE, SHIMADZU) with a thermal conductivity detector (TCD).

To evaluate the stability of Pt SAs/TiO_2, a 6-cycle experiment with a duration of 18 hours was performed. In the cycle experiment, the experimental parameters and conditions were maintained at the same level as the photocatalytic hydrogen performance test. After one cycle measurement, the reactor was re-purged with Ar and irradiated again for the second cycle. After repeating this process for six cycles, the

precipitation was washed with deionized water and ethanol, and then dried in an oven at 60 °C overnight for further characterization.

Theoretical DFT Calculations

The theoretical modelling of the TiO_2 systems was performed by density functional theory (DFT) in the gas phase by geometry optimization under constraint using an unrestricted BP86 functional with the Euler-Maclaurin-Lebedev grid (70, 302). The computational package used was Spartan 10 (Ver. 1.1.0, parallel version, Wavefunction Inc., Irvine, CA 92612). The SCF convergence and gradient convergence were set to 10^{-7} a.u. for the energy change and <0.0003, respectively. The structure template used for the TiO_2 models was taken from the X-ray structure of anatase phase (Howard C J, Sabine T M, 'Dickson. Structural and thermal parameters for rutile and anatase. Acta Crystallographica, Section B **1991**, *47*, 462-468). The minimal unit Ti (1,2,3) was taken and the position of the Ti centers were kept frozen in the models as those in the X-ray structure (Ti reciprocal distances) while the rest of atoms were left free during optimization. The position of interacting Pt^{2+} cation with the TiO_2 models was first assessed by semiempirical unrestricted PM3 method and then the structures were refined by DFT.

Results and Discussion

Table S1. STEM-EDX data for Pt SAs/TiO_2-F and Pt SAs/TiO_2-OH_1

Samples	**Ti (at%)**	**O (at%)**	**F (at%)**	**Pt (at%)**
Pt SAs/TiO_2-F	31.12	65.57	3.07	0.24
Pt SAs/TiO_2-OH_1	28.31	70.25	1.34	0.11

Table S2. AAS and SEM-EDX analysis for 0.005 mM Pt loading on the TiO_2 nanosheet without and with NaOH treatment

NaOH Treatment	**Pt (wt%)-AAS**	**Pt (at%)-SEM-EDX**
0h	0.13	0.05
8h	0.03	0.02
16h	0.02	0.02
24h	0.02	0.01

Table S3. XPS data for TiO_2 nanosheet without and with NaOH treatment

Atomic percentage	**C**	**O**	**F**	**Na**	**Ti**
0h	55.50	28.49	4.83	0.09	11.09
8h	52.86	32.35	1.17	1.59	12.02
16h	56.08	29.86	1.08	1.98	10.99
24h	56.17	30.53	0.88	1.45	10.97

Table S4. AAS, SEM-EDX and XPS analysis for Pt loading on TiO_2 nanosheet in different concentrations of Pt solutions and by different deposition methods

Sample	**Pt (wt%)-AAS**	**Pt (at%)-SEM-EDX**	**Pt (at%)-XPS**
0.001 mM Pt	0.02	0.11	0.03
0.005 mM Pt	0.12	0.15	0.05
0.01 mM Pt	0.30	0.18	0.27
0.05 mM Pt	1.87	0.65	0.5
0.005 mM-photodeposited Pt	0.20	0.37	0.14

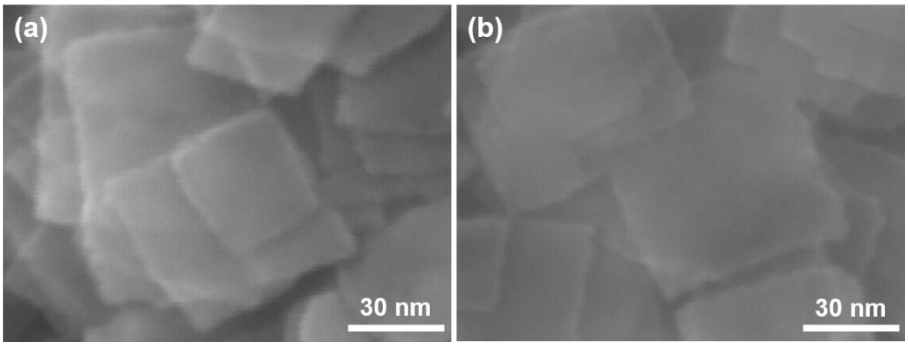

Figure S1. SEM images of: a) TiO_2-F; b) TiO_2-OH_1.

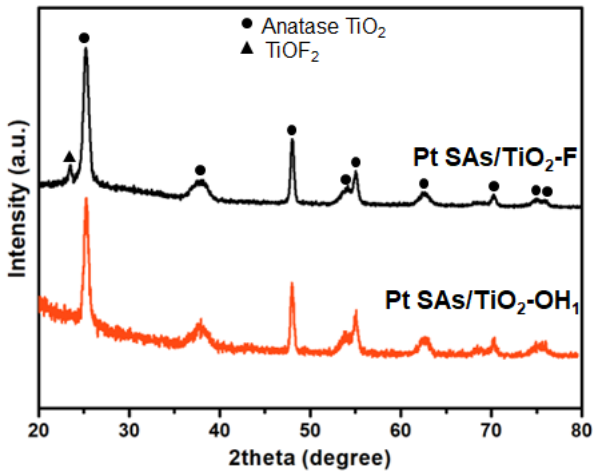

Figure S2. XRD patterns of Pt SA/TiO_2-F and Pt SA/TiO_2-OH_1.

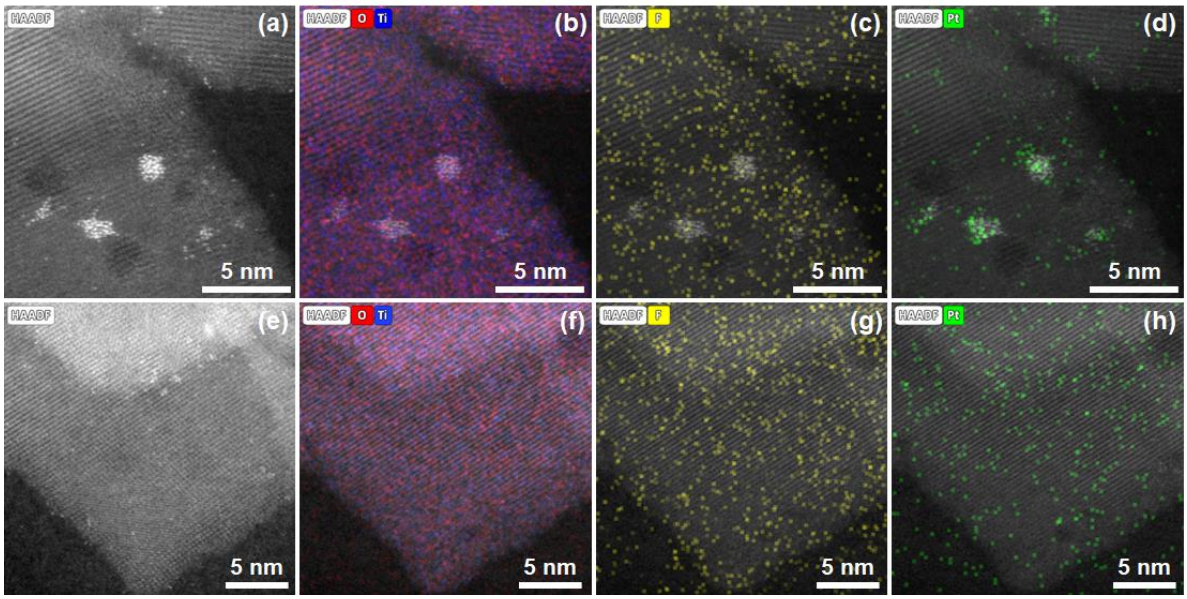

Figure S3. a-d) energy-dispersive X-ray element mappings of Pt SAs/TiO_2-F, e-h) energy-dispersive X-ray element mappings of Pt SAs/TiO_2-OH_1.

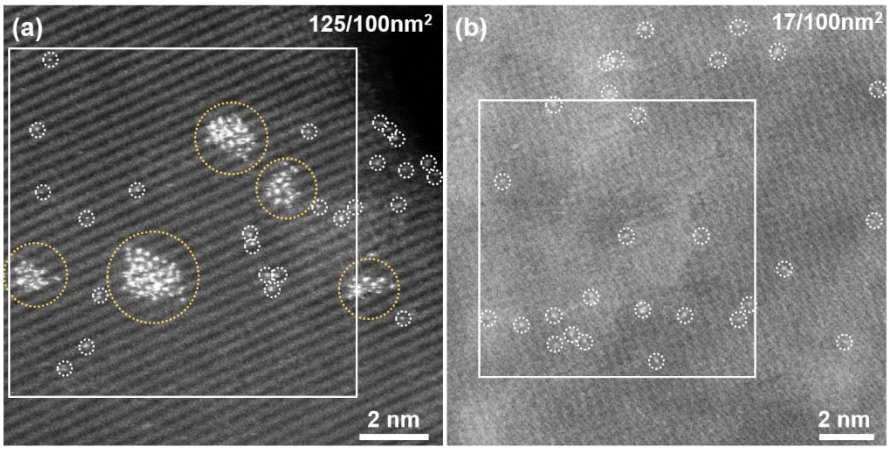

Figure S4. HAADF-STEM image of (a) Pt SAs/TiO_2-F, (b) Pt SAs/TiO_2-OH_1. The white squares (10 nm ×10 nm) represent the SA density calculation areas.

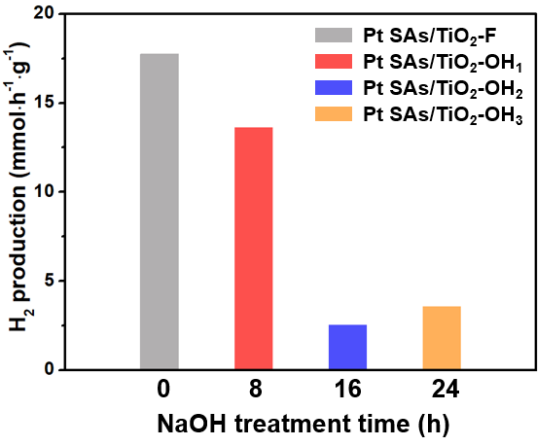

Figure S5. Photocatalytic H_2 evolution rate of Pt SAs on TiO_2 nanosheets with different NaOH treatment times.

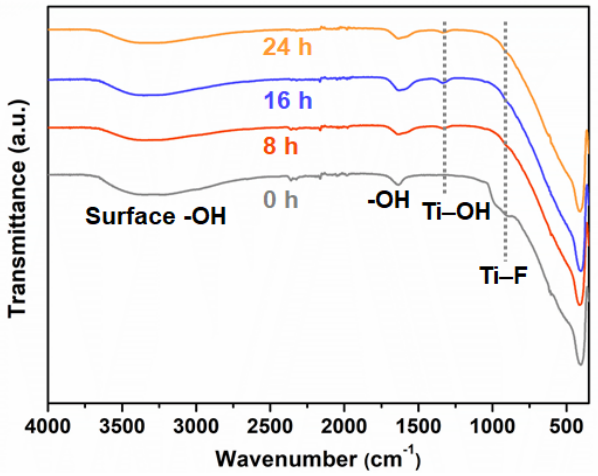

Figure S6. FTIR spectra of TiO_2 nanosheets with different NaOH treatment times.

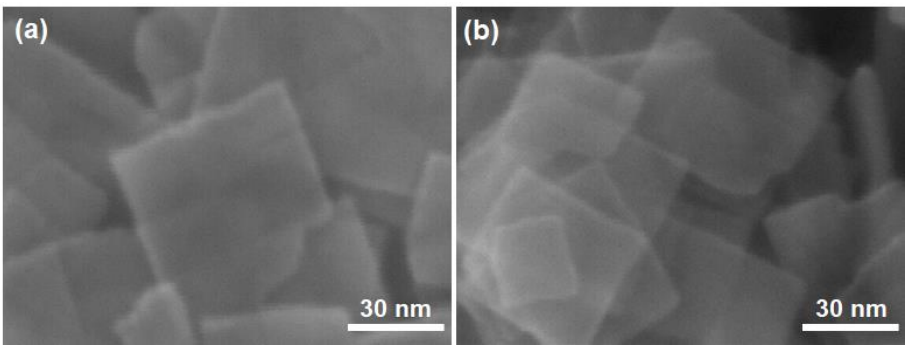

Figure S7. SEM images of (a) TiO_2-OH_2 and (b) TiO_2-OH_3.

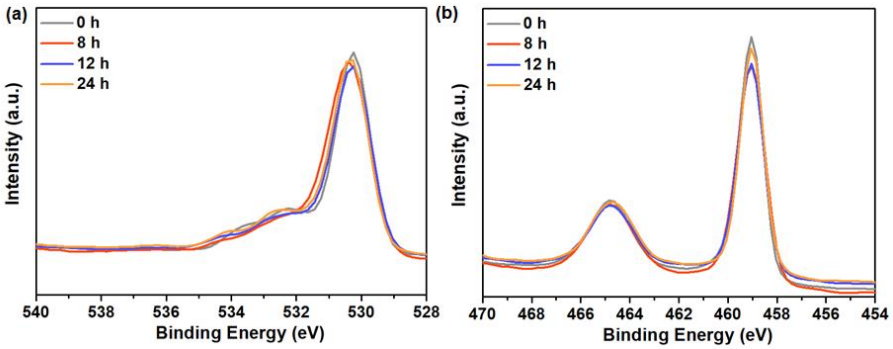

Figure S8. a) O 1s and b) Ti 2p XPS spectra of TiO_2-F, TiO_2-OH_1, TiO_2-OH_2 and TiO_2-OH_3.

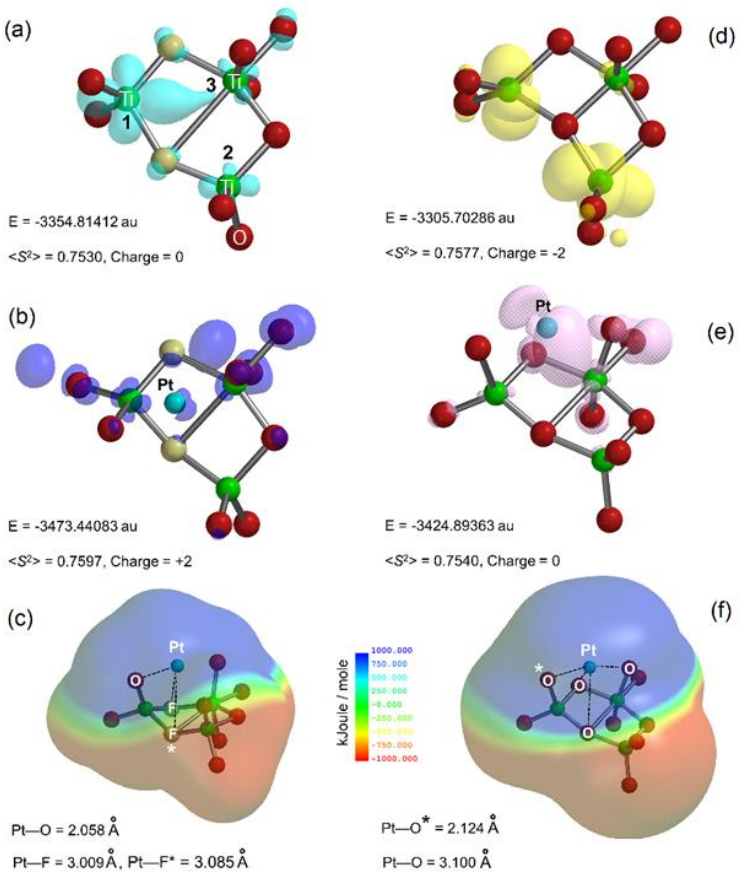

Figure S9. DFT geometry optimized theoretical models (gas phase) of TiO_2 systems, with and without F-doping, before and after interaction with single Pt^{2+} cation. H atoms are not displayed for clarity. (a) $Ti_3O_8F_2H_7$ computed with UBP86/6-31G* (S =1/2, charge = 0), (b) $PtTi_3O_8F_2H_7$ computed with UBP86/6-31G*/LANL2DZ (S =1/2, charge = 2), (d) $Ti_3O_{10}H_7$ computed with UBP86/6-31G*+ (S =1/2, charge = -2), (e) $PtTi_3O_{10}H_7$ computed with UBP86/6-31G*/LANL2DZ (S =1/2, charge = 0). In panel (a),(b),(d) and (e) the spin density isosurfaces are drawn at 0.002 isoval. Panel (c) and panel (f) show the electrostatic potential mapped surface of $PtTi_3O_8F_2H_7$ (c) and $PtTi_3O_{10}H_7$ (f).

Details to the DFT calculations.

The charge compensation phenomenon due to F doping is shown by theoretical modelling (DFT/UBP86/6-31G*, neutral, gas phase) using a small model system, $Ti_3O_8F_2H_7$ (Figure S9a), taking as structural template of the X-ray structure of anatase phase. Here, the labelled Ti(1) and Ti(2) centres are the Ti sites located on the surface (the under-coordinated sites) of TiO_2-F, while the Ti(3) site is associated to the lattice (see Figure S9a for labelling). Taking into consideration the results from NMR analysis, the theoretical model includes Ti_3-F and Ti_2-F□ coordination motives. The calculated spin density distribution for $S = ½$ shows that most of the spin is localized on the Ti(1) site and this is the position that may preferentially interact with the Pt cation upon doping (*vide infra*). For comparison, in Figure S9d is shown the same Ti_3 model without F^- doping ($Ti_3O_{10}H_7$), having similarly $S = ½$ configuration, but without charge balance. In this scenario, both Ti(1) and Ti(2) sites located on the surface equally shares the majority of spin density.

The occurrence of galvanic displacement reaction process is supported by theory using the model system $PtTi_3O_8F_2H_7$ (Figure S9b, DFT/UBP86/6-31G*/LANL2DZ, charge = +2, gas phase) where it is evident the occurrence of spin transfer from Ti^{3+} site/s to the interacting Pt^{2+} cation, being accompanied by substantial reorganization of the S=1/2 spin distribution in favour of oxygen and fluorine residues. Here the calculated

Mulliken spin and Mulliken charge in Pt accounts for 0.21 a.u. and ~ 0.04 a.u., respectively. It should be noted that the galvanic displacement, as process, seems to occur effectively also in $Ti_3O_{10}H_7$ upon interaction with Pt^{2+} ($PtTi_3O_8H_7$, Figure S9e, DFT/UBP86/6-31G*/LANL2DZ, charge = 0, gas phase), giving calculated Mulliken spin and Mulliken charge in Pt of 0.67 a.u. and ~ 0.03 a.u., respectively. The electrostatic potential maps for both Pt models ($PtTi_3O_8F_2H_7$ and $PtTi_3O_{10}H_7$) are shown in Figure S9c and S9f respectively, highlighting the extend of positive charges region around Pt cation.

Overall, although the galvanic process appears to take place in TiO_2 system with Pt doping without the presence of F in the TiO_2 structure, it seems the galvanic displacement process is energetically favored in fluoride free titania but kinetically favored in F-containing titania.

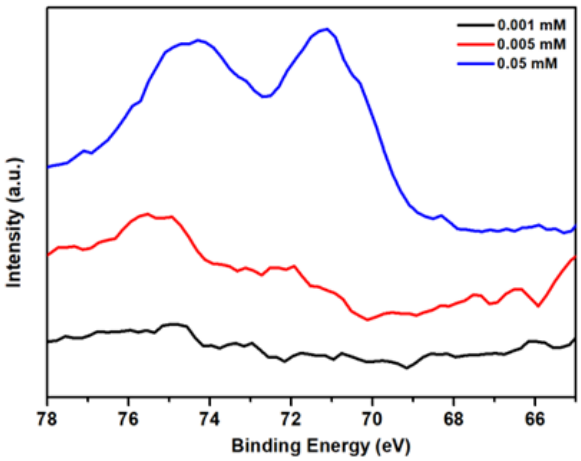

Figure S10. High-resolution XPS spectra of Pt 4f of TiO_2 nanosheets after dark deposition in different concentrations of Pt solutions.

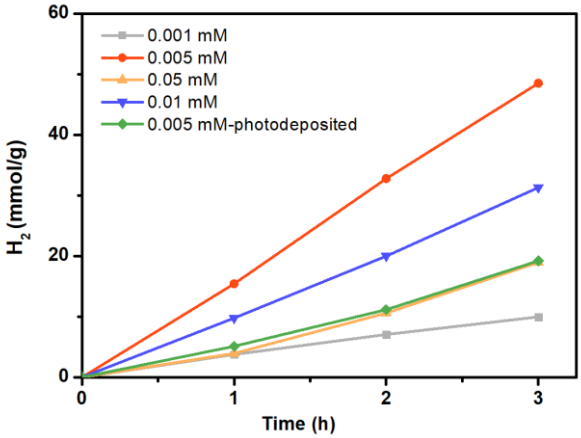

Figure S11. Photocatalytic H_2 production of TiO_2 nanosheets after dark deposition in different concentrations of Pt solutions (from 0.001 to 0.05 mM), and that of TiO_2 nanosheet after photodeposition in a 0.005 mM Pt solution.

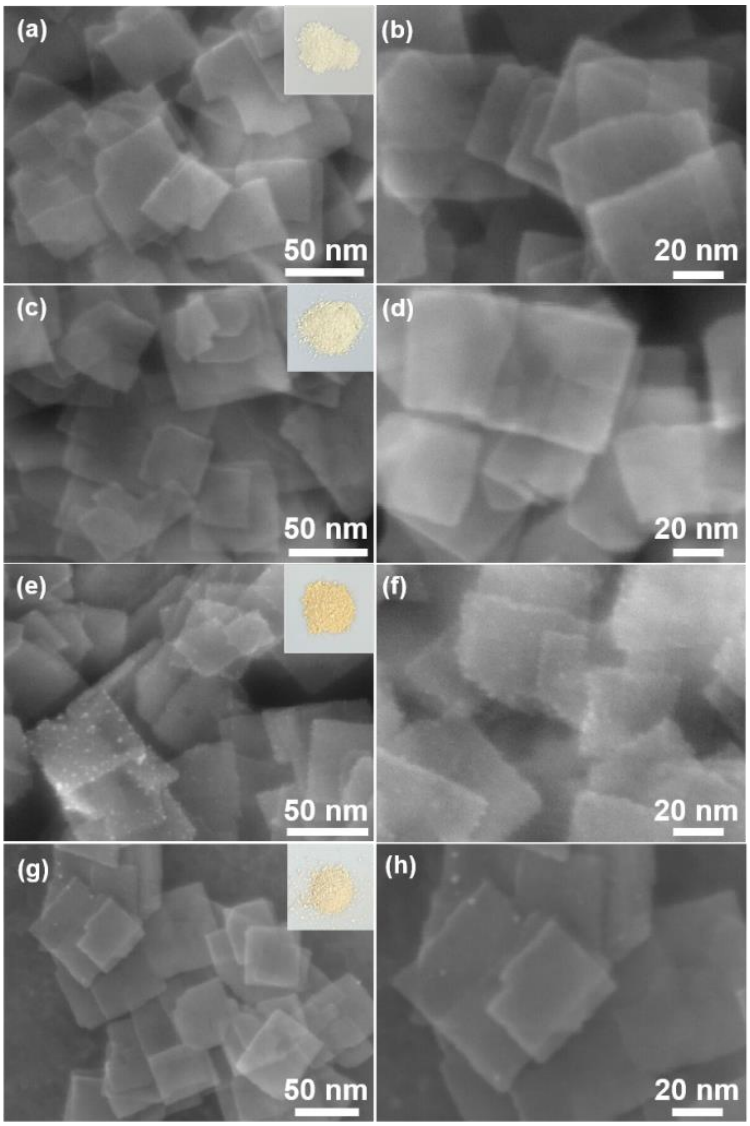

Figure S12. SEM images of a,b) TiO_2 nanosheets with dark deposition in 0.001 mM Pt, c,d) TiO_2 nanosheets with dark deposition in 0.01 mM Pt, e,f) TiO_2 nanosheets with dark deposition in 0.05 mM Pt, g,h) TiO_2 nanosheets with photodeposition in 0.005 mM Pt. Insets are the optical photographs of the samples.

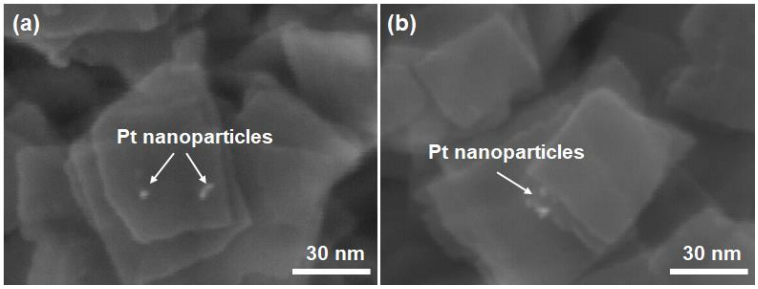

Figure S13. a, b) SEM images of Pt deposited on TiO_2-F and illuminated under UV light for 18 h.

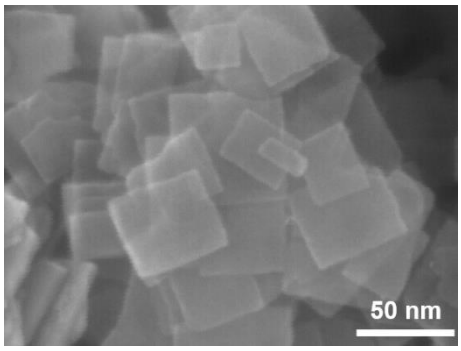

Figure S14. SEM images of Pt SAs/TiO_2 after photocatalytic H_2 evolution test for 6 cycles.

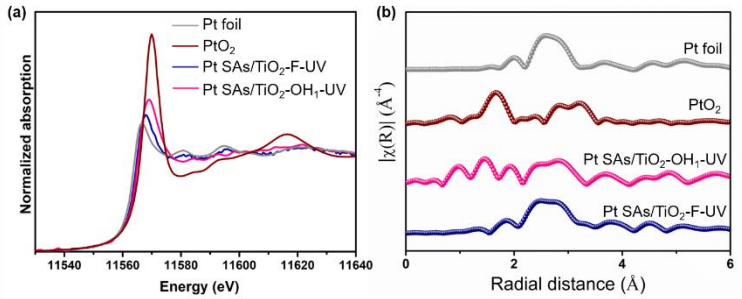

Figure S15. Characterization of illuminated samples. a) XANES spectra at the Pt L_3 edge of Pt SAs/TiO_2-F-UV and Pt SAs/TiO_2-OH_1-UV. b) Fourier transform EXAFS spectra (R-space) of Pt SAs/TiO_2-F-UV and Pt SAs/TiO_2-OH_1-UV.

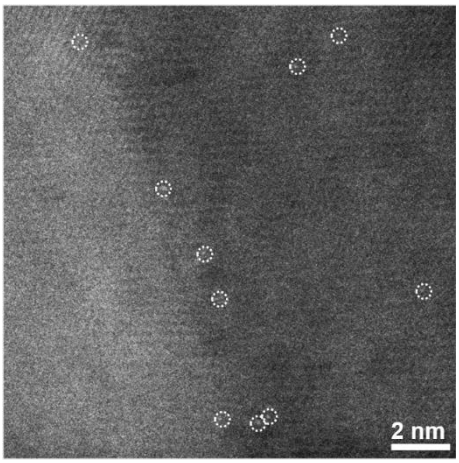

Figure S16. HAADF-STEM image of Pt SAs/TiO_2-OH_1-UV.